PHYSICAL REVIEW A VOLUME 55, NUMBER 6 JUNE 1997

Extension of classical trajectory Monte Carlo calculations to ion–Rydberg-atom collisions in a magnetic field

S. Bradenbrink, E. Y. Sidky,* Z. Roller-Lutz, H. Reihl, and H. O. Lutz
Fakultät für Physik, University of Bielefeld, Postfach 100131, D-33501 Bielefeld, Germany

(Received 6 January 1997)

Theoretical electron transfer cross sections for 1.3–130 eV/amu singly charged ions colliding with Rydberg atoms ($n=28$, $m=2$) in a magnetic field up to 4 T are presented. Both paramagnetic and diamagnetic interactions are taken into account for the initial state and the collision. Cross sections are calculated within the classical trajectory Monte Carlo model. A method to create a classical ensemble of electrons in a nonseparable Hamiltonian allows the initial quantum stationary states to be modeled. The effect of the magnetic field on electron capture is analyzed in terms of the field-induced alteration of the initial state, as well as the direct influence on the collision dynamics. [S1050-2947(97)09606-6]

PACS number(s): 34.60.+z, 32.60.+i, 34.70.+e

I. INTRODUCTION

One hundred years after the work of Zeeman [1] there are still unresolved problems concerning atomic processes in a magnetic field. Many of the theoretical efforts are focused on astrophysical problems involving extremely high magnetic fields as can be found around white dwarfs ($B\approx 10^2-10^5$ T) or neutron stars ($B\approx 10^7-10^9$ T). The main reason for this is that only at such high magnetic field strengths is the magnetic energy equal to or greater than the Coulomb energy for ground-state atoms. There have been some calculations for ion-atom collisions at such field strengths [2–5]. In contrast for a typical laboratory field with a strength of a few Tesla, the diamagnetic energy becomes comparable to the Coulomb energy if the atoms are excited to high Rydberg states, and therefore such a field exerts a nontrivial influence on ion–Rydberg-atom collisions.

In this paper we follow up our earlier work [6] with a more detailed account of the theoretical method as well as numerically calculated cross sections for charge exchange in a magnetic field up to 4 T. For the initial Rydberg state we choose a principal quantum number $n=28$, $m=2$. In this case the ratio of magnetic energy to Coulomb energy is of the order 0.1 and therefore n is still a good quantum number, but l is no longer. The l-mixing region is experimentally accessible, but presently there are, as far as we know, no beam experiments that study this system even though this process is ubiquitous in plasma physics. The numerical results presented in this paper illuminate the effect of an applied magnetic field on the ion-atom collision by comparing with calculated cross sections for the field-free case. The calculations were performed with a CTMC (classical trajectory Monte Carlo) method, modified to allow for complications from magnetic field effects.

Collision energies of the singly charged ion range between 1.3 and 130 eV/amu, corresponding to reduced velocities $v_r=v/v_e$ between 0.2 and 2 (v is the collision velocity; $v_e=n^{-1}$ a.u. is the Bohr orbital electron velocity). Atomic units are used throughout this paper unless explicitly stated.

II. THEORETICAL APPROACH

In principle one must solve the equations of motion for three interacting bodies, but due to the relative speed of the ion and target atom and the lightness of the electron compared to the atomic nuclei standard approximations can be employed to simplify the system. The projectile ion moves at a constant velocity $\vec{v}$ and the target nucleus remains motionless. The Hamiltonian governing the active electron is then

$$H=\frac{1}{2}\vec{p}^2-\frac{1}{|\vec{r}|}-\frac{1}{|\vec{r}-\vec{R}|}+\frac{1}{2}\gamma l_z+\frac{1}{8}\gamma^2\rho^2, \tag{2.1}$$

where $\vec{R}=\vec{b}+\vec{v}t$ is the internuclear vector, $\vec{b}$ is the impact parameter, and $\vec{v}$ is the ion velocity in the target frame chosen parallel with the magnetic field (z axis); see Fig. 1. l_z is the z component of the electron angular momentum. $\gamma=B/(2.3505\times 10^5\ \mathrm{T})$, where B is the magnetic field strength expressed in Tesla. The magnetic-field terms are expressed with the Coulomb symmetric gauge with respect to the target nucleus. We are interested in the l-mixing region, where the diamagnetic energy $\gamma^2\rho^2/8$ is small compared to the Coulomb binding energy (less than 10%) and perturbation theories are applicable. Figure 2 shows a contour plot of the potential generated by the target-projectile system. The potential contours in the figure are selected at typical electron energies during the collision process. Due to the cylindrical symmetry of the magnetic field the circular contours of the target Coulomb potential are compressed transverse to the magnetic field.

To calculate the cross sections for ion–Rydberg-atom collisions in a magnetic field we use the established CTMC method, modified to allow for the magnetic field. The CTMC method is nonperturbative and explicitly considers all classical three-body and three-dimensional effects, but does not account for tunneling or interference. Such three-body systems involving highly excited states can be solved quantum mechanically only with severe approximations, while the

---

*Present address: Department of Physics, Kansas State University, Manhattan, KS 66506.

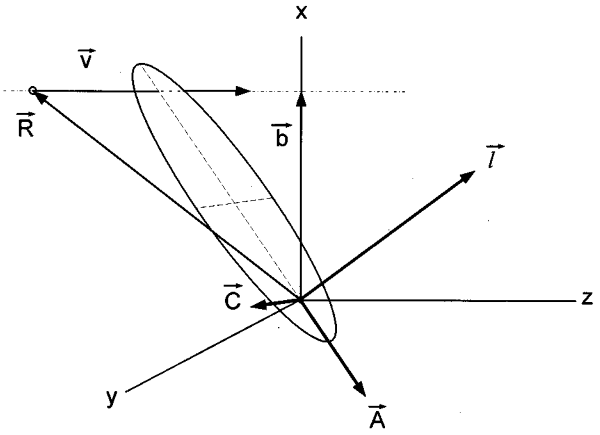

FIG. 1. Schematic of the ion-atom interaction shown in the collision frame. $\vec{R}$ is the internuclear vector, $\vec{b}$ is the classical impact parameter, and $\vec{v}$ is the projectile velocity. The magnetic field is parallel to the z direction. Also shown is an example of a Kepler ellipse with the angular momentum $\vec{l}$, Runge-Lenz vector $\vec{A}$, and $\vec{C}=\vec{l}\times\vec{A}$ shown schematically. For orientation the dashed lines indicate the major and minor axes.

Newton's equations for regular three-body systems can be solved numerically to any desired degree of accuracy on modern computers. The basic principle of the CTMC method is the validity of a generalized correspondence principle, which states that for sufficiently high quantum numbers the exact quantum state can be approximated by a classical ensemble [7]. The calculation of the physical observables (e.g., cross section for ionization, exchange, and excitation) is done by averaging over a great number of randomly chosen trajectories. This method has been successfully applied to numerous collision systems, especially systems involving Rydberg atoms [8–10].

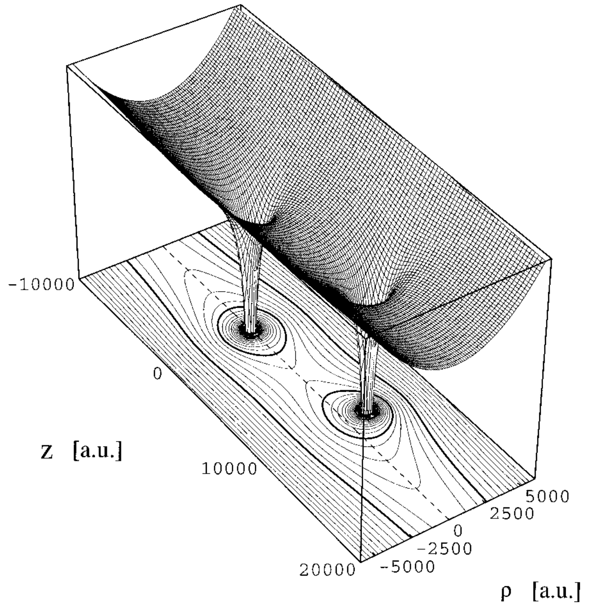

FIG. 2. Surface plot and corresponding contour plot of the potential from the target and projectile nuclei including the diamagnetic interaction. The target rests at the origin and the projectile is at a distance z of 10 000 a.u. (atomic units) with an impact parameter of 1500 a.u. The bold contours represent the energy of the initial electron and the zero energy. The dashed line marks the symmetry axes. Spacing of the contours is 0.0001 a.u.

The CTMC method consists of three parts: (1) the classical generation of the target electron distribution, (2) integration of Newton's equations, and (3) the classification of the various processes after the collision. Due to the applied magnetic field steps (1) and (3) require new procedures. The classical representation of the target atom is the main problem of the CTMC method [11]. The magnetic field distorts the electron starting distribution and up to now no method has been published to construct an electron distribution for a Rydberg atom in a magnetic field for the l-mixing region, which is described by a nonseparable Hamiltonian. To construct a classical microcanonical ensemble of initial-state electrons, presented in Sec. II A, we need the energy eigenvalue, a new integral of motion, and the magnetron period τ_{mag} calculated in the frame of degenerate perturbation theory outlined in Secs. II A 1 and II A 2. The applied magnetic field also changes the dynamical properties of the system, represented by the equation of motions resulting from the Hamiltonian (2.1). Finally due to the diamagnetic energy a new characterization of the exchange and ionization processes is required; see Sec. II B.

A. Initial-state method

We present a method to generate a classical microcanonical ensemble for a quasi-integrable initial-state Hamiltonian:

$$H_{\mathrm{init}}=H_0+V. \tag{2.2}$$

The term H_0 represents a zeroth-order Hamiltonian that is integrable, and V represents a small perturbation that introduces nonseparability into H_{init}. The magnitude of V is small enough that the classical orbits of H_{init} are still regular, and thus one can derive approximate constants of motion that replace constants of the motion for H_0. Equation (2.2) is analyzed first by quantum-mechanical degenerate perturbation theory in order to classify and generate probability distributions for the new set of stationary eigenstates. Analysis of Eq. (2.2) with classical perturbation theory provides information necessary for the actual construction of the initial-state ensembles, which model the quantum-mechanical probability distributions as closely as possible.

The discussion of the initial-state method proceeds with the specific problem where H_0 represents the Rydberg atom under the linear Zeeman effect, and V is the diamagnetic interaction:

$$H_0=\frac{1}{2}\,\vec{p}^2-\frac{1}{|\vec{r}|}+\frac{1}{2}\,\gamma l_z, \tag{2.3}$$

$$V=\frac{1}{8}\,\gamma^2\rho^2. \tag{2.4}$$

However, this method can be generalized to other systems of the form in Eq. (2.2). For the calculations presented here the magnetic field is at most 4 T, and the initial target state is excited to the $n=28$ manifold. For these parameters the electron orbit is a combination of the fast elliptical motion, an intermediate cyclotron motion, and a slow oscillation (magnetron motion with period $\tau_{\rm mag}$ [6]). Classically, the scaled energy $\epsilon = E\gamma^{-2/3}$ is -0.96, which characterizes regular classical dynamics [12]. Before going on to the details of the classical ensemble generation we summarize the perturbative theory for a Rydberg atom in a magnetic field, distilled from Refs. [13–15].

1. Quantum-mechanical perturbation theory

To find the target atomic-state characteristics and energy spectrum a quantum-mechanical analysis of a Rydberg atom in a magnetic field is necessary. References [13,14] give a detailed analysis of the diamagnetic Rydberg atom in the l-mixing regime. Eigenstates are found by diagonalizing the diamagnetic potential within a single n manifold:

$$\begin{aligned} U_{ll'} &= \frac{1}{8}\gamma^2 \langle nlm|r^2\sin^2\theta|nl'm\rangle \\ &= \frac{1}{8}\gamma^2 \sum_{k=0}^{n-|m|-1} \langle l|k\rangle \epsilon_k \langle k|l'\rangle, \end{aligned} \tag{2.5}$$

$$\psi_k(r,\theta,\phi) = \sum_l \langle k|l\rangle f_{nl}(r) Y_{lm}(\theta,\phi), \tag{2.6}$$

where f and Y represent the radial Coulomb functions and spherical harmonics, respectively. The expansion coefficients $\langle k|l\rangle$ give the perturbative eigenstates of $H_{\rm init}$, and ϵ_k is the respective energy shift. Note that the eigenstates from the diagonalization in Eq. (2.5) are independent of field strength.

The manifold of eigenstates that emerge from the diagonalization of Eq. (2.5) split into two types of states. Those corresponding to the lower set of energy eigenvalues ϵ_k (by convention the maximum k corresponds to the minimum ϵ_k) are localized along the magnetic field. The higher-energy states (lower k) resemble a disk perpendicular to the magnetic field, and their spectrum is akin to an inverted harmonic oscillator; the highest-energy state has a minimum number of nodes [13,14]. Our task is to approximate the probability distributions $\psi_k\psi_k^*$ and energy eigenvalues ϵ_k as closely as possible by a stationary classical ensemble.

2. Classical perturbation theory

Before discussing how to construct the initial-state ensemble it is necessary to develop further the classical treatment of the diamagnetic Rydberg atom presented in [15]. In performing the classical perturbation theory the electron trajectories are viewed as primarily elliptical, the exact trajectories of H_0 in Eq. (2.3). The diamagnetic potential of Eq. (2.4) is regarded as a perturbation that causes a slow, oscillatory drift of the angular momentum vector $\vec{l}$ and the Runge-Lenz vector $\vec{A}$ (magnetron motion: ‘‘pulsing and wobbling’’ of the classical ellipse). The period of this oscillation $\tau_{\rm mag}$ is a key parameter needed for the construction of the classical ensemble.

To calculate the drift of the elliptical parameters the effect of the perturbing potential V is averaged over one elliptical period. As in [15] we write the trajectory of the Kepler ellipse in terms of the constants of the elliptical motion $\vec{l}$ and $\vec{A}$:

$$\vec{r}(t) = x_0(t)\vec{A}/e + y_0(t)\vec{C}/(le), \tag{2.7}$$

where

$$\begin{gathered} x_0(t) = Q(\cos\xi - e), \quad y_0(t) = Q(1-e^2)^{1/2}\sin\xi, \\ \vec{C} = \vec{l}\times\vec{A}, \end{gathered} \tag{2.8}$$

the eccentricity e is the magnitude of the Runge-Lenz vector $\vec{A}$, Q is the semimajor axis, and ξ is the Kepler anomaly. Applying time-dependent perturbation theory [15] gives the drift of $\vec{A}$ and $\vec{l}$ averaged over the elliptical orbit:

$$\frac{d\vec{l}}{dt} = \frac{Q^4\gamma^2}{8}\left\{ \frac{4e^2+1}{e^2} A_z[\vec{A}\times\hat{z}] + \frac{1-e^2}{l^2e^2} C_z[\vec{C}\times\hat{z}] \right\}, \tag{2.9}$$

$$\begin{aligned} \frac{d\vec{A}}{dt} = &-\frac{Q^{3/2}\gamma^2}{8}\frac{\sqrt{1-e^2}}{le^2} \\ &\times\{(3e^2-4A_z^2)\vec{C} + C_z(e^2\hat{z}+4A_z\vec{A})\}. \end{aligned} \tag{2.10}$$

[Equation (5) of [15] was found to be slightly inaccurate and hence is rewritten correctly in Eqs. (2.9) and (2.10).] Equation (2.9) implies that l_z is still a constant of motion, and two other approximate constants of motion emerge from Eqs. (2.9) and (2.10):

$$Q = \frac{l^2}{1-e^2}, \tag{2.11}$$

$$\Lambda = 4e^2 - 5A_z^2. \tag{2.12}$$

Conservation of l_z reflects that $H_{\rm init}$ is independent of ϕ, and approximate conservation of Q implies that the path that the electron follows at any one instant is approximately following an ellipse corresponding to the energy $-1/(2Q)$. Λ is really a new quantity arising from the particular form of the diamagnetic potential. Orbits corresponding to negative values of Λ are stretched along the magnetic field as with the high k values from the quantum mechanical perturbation theory, and positive Λ correspond to the low-k values, i.e., a disklike distribution perpendicular to the magnetic field.

To find the magnetron period $\tau_{\rm mag}$ one integrates Eqs. (2.9) and (2.10) after some simplification. These two equations represent six coupled differential equations, but they can be reduced to two coupled differential equations by taking advantage of the three new constants of motion as well as the orthogonality of the angular momentum and Runge-Lenz vector, $\vec{l}\cdot\vec{A}=0$. We reduce to the coupled equations:

$$\frac{dA_z}{dt} = -\frac{Q\gamma^2}{2} C_z, \tag{2.13}$$

$$\frac{dC_z}{dt} = \frac{Q^2\gamma^2}{8e^2} A_z\left(e^4 + \Lambda - \frac{5C_z^2}{n^2}\right). \tag{2.14}$$

Note that for simplicity e still appears in Eq. (2.14), but it is related to A_z through Λ. The field strength can be eliminated from Eqs. (2.13) and (2.14) by going to scaled time $t' = t\gamma^2$. For a given eigenstate k, τ_{mag} (in a.u.) is found by integrating Eqs. (2.13) and (2.14) with the constants of motion set to $l_z = m$, $Q = n^2$, and $\Lambda = (\epsilon_k - n^2 - m^2)/n^2$ [14].

3. Generation of the classical ensemble

We present now a detailed method for generating an electron starting distribution in a magnetic field for the l-mixing region, based on the results of the quantum-mechanical and classical perturbation theory. Since none of the quantum numbers n, m, and k, which characterize the target Rydberg state, are degenerate, no binning is performed for the corresponding classical constants of motion Q, l_z, and Λ, because we wish to model the initial state with a microcanonical ensemble. To produce electron starting distributions that mimic the quantum ones from Eq. (2.6), one distributes the initial-state electrons according to a probability distribution proportional to $1/|\vec{v}|$ along the set of classical orbits with l_z, Q, and Λ, corresponding to a specific quantum-mechanical k state. The velocity of the Runge-Lenz and angular momentum ϕ component is constant as the orbit precesses about the field axis due to the paramagnetic interaction. Selecting ϕ_l randomly in $[0,2\pi]$ specifies a unique orbit (ϕ_A is dependent on ϕ_l through $\vec{A}\cdot\vec{l} = 0$).

One strategy would be to distribute the electrons by starting them at the same phase space point and propagate Hamilton's equations with H_{init} for a randomly chosen time t. This automatically would give a $1/|\vec{v}|$ distribution, and avoid the necessity of an analytic expression for the electron trajectory. This method fails, since t should be selected between 0 and the recurrence time, which is infinite as the electron path fills a region of phase space densely. One can, however, divide the trajectory into the elliptical and magnetron motions by selecting the electron coordinate randomly on an unperturbed ellipse and evolving the electron according to H_{init} for t randomly selected in $[0,\tau_{\mathrm{mag}}]$. This method allows the electron to reach any point along its true trajectory, and thus creates the desired microcanonical ensemble.

To randomly place the electron using the field-free ellipse, one must first define the ellipse by specifying $\vec{A}$ and $\vec{l}$. The magnitude of the angular momentum varies as the electron executes its motion, thus its initial choice is not critical as long as l lies in the range of accessible values for a given Λ. Taking $\langle k|l|k\rangle$ for the initial l value fulfills this requirement. l_z is fixed, since we are only interested in $m=2$, and as stated earlier ϕ_l is selected randomly. The magnitude e of the Runge-Lenz vector follows from the relation for Q in Eq. (2.11), and the z component A_z is determined up to sign with Λ in Eq. (2.12). Finally, ϕ_A is found by orthogonality between $\vec{A}$ and $\vec{l}$.

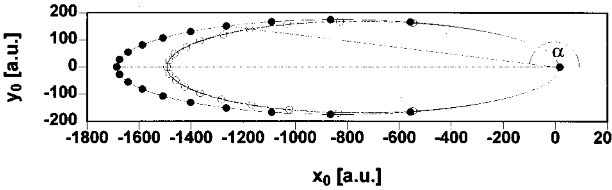

FIG. 3. The solid curve represents an ellipse of eccentricity $e = 0.977$ ($l = 6$ and $n = 28$), where the filled circles are equally spaced in time. The dashed curve displays the corresponding energy corrected coordinates; the solid line indicates constant ξ and α is the mean anamoly. The axes shown are in the frame of the original ellips, and the nucleus rests at x_0, $y_0 = 0$.

In practice the electron is randomly placed on an ellipse oriented in the coordinate xy plane with the aphelion on the negative x axis. The size and shape of the ellipse are determined by l and e, and the starting point on the ellipse is chosen by selecting a mean anomaly α in $[0,2\pi]$, which determines the Kepler anamoly ξ through [16]

$$\alpha = \xi - e\ \sin\xi. \tag{2.15}$$

The proper orientation is accomplished by three rotations through the angles

$$\theta_l = \cos^{-1}\frac{l_z}{l}, \tag{2.16}$$

$$\varphi = \cos^{-1}\left(\pm\frac{A_z}{e\ \sin\theta_l}\right), \tag{2.17}$$

and ϕ_l. The first rotation θ_l about the y axis gives the electron the proper z component of angular momentum. The second rotation φ about the angular momentum vector $\vec{l}$ fixes the z component of the Runge-Lenz vector. The plus or minus in Eq. (2.17) indicates that the sign of A_z should be chosen randomly. The final rotation about the space fixed z axis gives the randomly chosen ϕ_l angle.

Due to the perturbing diamagnetic potential the random placement of the electrons on a predefined ellipse must be adjusted. The electrons up until now have distributed along a trajectory of H_0, but V introduces, in general, a small variation in the energy of the particles. In the case of diamagnetism electrons at larger ρ will experience a boost in energy due to the ρ^2 potential. This must be corrected in order to obtain a microcanonical ensemble. The parameter to adjust is the semimajor axis Q, which is directly related to the energy, and this can be actuated by either changing l or e. We adjust l by

$$l' = l\left(1 + \frac{2l^2}{1-e^2}\,\frac{1}{8}\ \gamma^2\rho^2\right)^{-1/2}, \tag{2.18}$$

where l, e, and ρ refer to the uncorrected electron, and l' is the adjusted angular momentum. Having changed l, the position of the electron is recalculated keeping e, A_z, l_z, ϕ_l, and ξ fixed. Performing this energy correction puts the electron on a slightly different Kepler ellipse, shifting the ρ coordinate and subsequently affecting the diamagnetic energy. Thus the correction must be performed recursively. After ten recursions the initial electron energy has a relative error 10^{-7} of the quantum energy eigenvalue. The effect of the energy correction is illustrated in Fig. 3. The energy correction shown in the figure is an extreme case for a 4-T field, since it is the starting ellipse for the k_{min} state that is greatly affected by the magnetic field.

The last step in simulating the microcanonical ensemble, as mentioned earlier, is to evolve the electron coordinates according to H_{init} for a time t varying randomly between zero and τ_{mag}. We calculate τ_{mag}, from Eqs. (2.9) and (2.10), for the k states that we wish to examine, namely, the minimum and maximum k values for a two-photon excita-

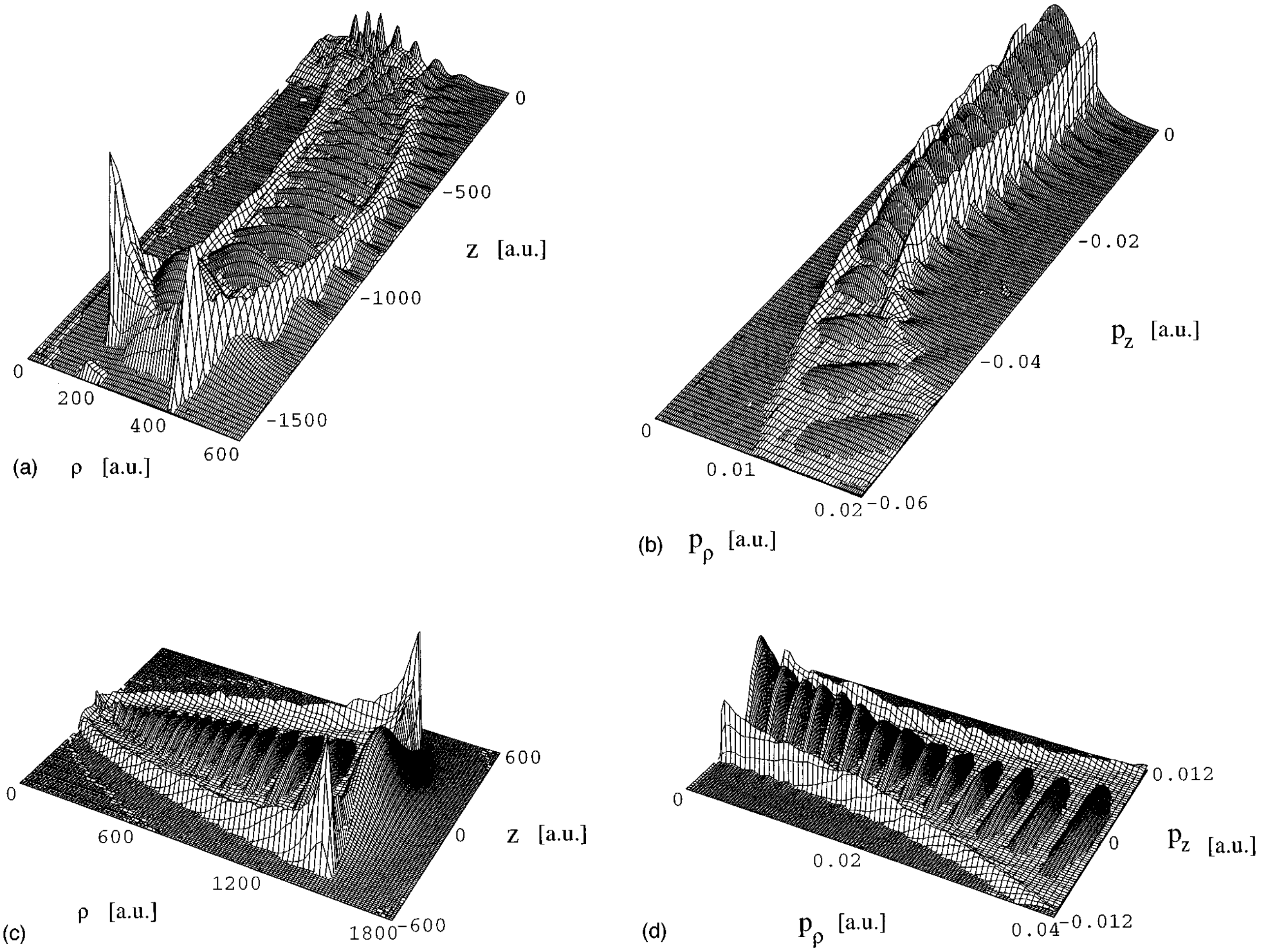

FIG. 4. Configuration space distribution (left) and momentum distribution (right) with $n=28$, $m=2$ for $k_{\max}$ (upper) and $k_{\min}$ (lower). Quantum-mechanical (high resolution grid) and classical ensemble distribution (low resolution grid) are shown in cylindrical coordinates; due to symmetry $k_{\max}$ is represented only for $z<0$ and $p_z<0$.

tion to $n=28$. Focusing on $m=2$ states, one finds that $k_{\max}=24$ and $k_{\min}=0$, since k must correspond to an even parity state. The magnetron period scales with the square of field strength:

$$\tau_{\rm mag}=\tau_0^k/B^2, \tag{2.19}$$

where

$$\tau_0^{k=24}=3.3344\times 10^7 \ \ (\text{a.u. T}^2), \tag{2.20}$$

$$\tau_0^{k=0}=2.9692\times 10^7 \ \ (\text{a.u. T}^2). \tag{2.21}$$

For comparison the orbital period for an $n=28$ electron is 1.4×10^5 a.u. [Note that if the classical perturbation results were not known, the period of the oscillations due to the perturbing potential V could still be found empirically by numerically evolving a constant of motion Ω from H_0 with the Hamilton's equations for $H_{\rm init}$, provided that $[H_{\rm init},\Omega]\neq 0$. Indeed this provides a good criterion for the validity of Eq. (2.19).] The resulting normalized distributions for $k_{\max}$ and $k_{\min}$ in configuration and momentum space are shown in Fig. 4. The method for generating the microcanonical ensemble is tested empirically simply by propagating the distributions in time and observing that they are stationary within the normal statistical fluctuations.

Also shown in Fig. 4 is the comparison of the classical ensembles with the corresponding quantum probability distributions. The regions of configuration and momentum space occupied by both the classical and quantum distributions agree very well. Also the probability amplitudes have matching radial dependence in both configuration and momentum space, aside from the behavior for r larger than the classical turning point (CTP) where the classical distribution must go to zero. The behavior transverse to the radial direction is noticeably different. The reason for this goes back to the correspondence principle, which states that there should be good agreement between classical and quantum mechanics for large quantum numbers. However, the states $k_{\max}$ and $k_{\min}$, displayed in Fig. 4, are likened to the extremal states of a harmonic oscillator and an inverted harmonic oscillator, respectively [13,14]. Both cases correspond to states with one transverse mode, so one would not expect the correspondence principle to hold exactly. Indeed the θ dependence of the classical probability distributions are dominated by CTP behavior, reflected by two ridges running along the caustics. A similar comparison is seen in the distribution of l, conjugate to θ, seen in Fig. 5. An attempt to minimize the

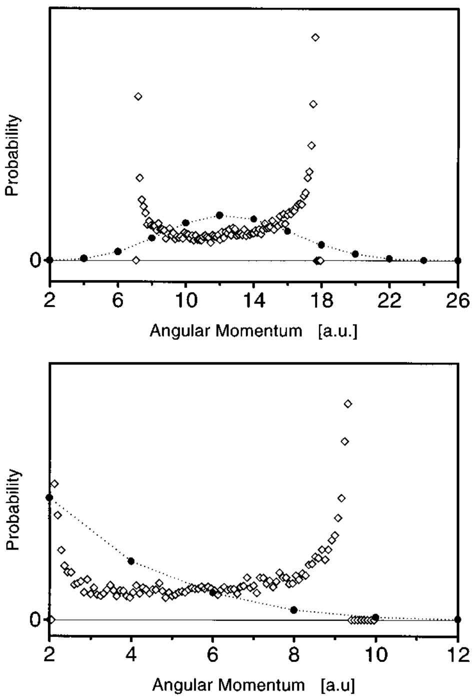

FIG. 5. Angular-momentum probability distribution for $k_{\max}$ (upper) and $k_{\min}$ (lower). The solid circles connected by the dashed lines represent the quantum probabilites, while the open diamonds are the corresponding classical ensemble l distribution. The lower l limit is defined by the choice of magnetic quantum number $m=2$.

discrepancy between the quantum and classical distributions was made by enforcing the quantum-mechanical l distribution from the outset. This, however, resulted in a nonstationary classical ensemble that eventually, not surprisingly, led back to the former classical l distribution. The effect of the difference between the classical and quantum distributions will be discussed after presenting the total cross sections for capture in Sec. III.

The other part of the initial wave function that one must model is the incoming plane wave for the projectile ion, for which we use a standard distribution [17]. We briefly describe its specific application here. The initial condition of the projectile in the collision frame is specified by its velocity $\vec{v}$, its impact parameter b, and the distance z_0 from the target. The ion velocity $\vec{v}$ is chosen parallel with the magnetic field (z axis) and lies in the xz plane. To reproduce a uniform flux of monoenergetic incident particles, the impact parameter of the projectile is chosen randomly by selecting b^2 out of the interval $[0,b_{\max}^2]$, where $b_{\max}$ is the impact parameter above which no ionization and capture processes occur. $b_{\max}$ depends on the target state and the ion velocity and has to be chosen properly, because when $b_{\max}$ is too large this will result in poor statistics while a smaller value of $b_{\max}$ will distort the results. Typical values of $b_{\max}$ in our system are ≈ 3500 a.u. The distance z_0 of the projectile is typically -4×10^4 a.u. and guarantees that the cross sections are independent of starting position, which indicates that the projectile-electron interaction is negligible compared to the target-electron interaction at the outset.

B. Integration of Hamilton's equations and final-state classification

After propagating the electron out to its randomly chosen position, we proceed by integrating Hamilton's equations of motion according to Eq. (2.1) with the ion starting at z_0. In performing the integration by a standard Runge-Kutta method with an adaptive step size the target center is taken as space fixed and the projectile moves along a straight line trajectory. Both of these simplifications reduce the number and complexity (e.g., motional Stark effect [18]) of the governing equations without introducing a noticeable error in calculating the total cross sections. After propagating Hamilton's equations such that the projectile is at an asymptotic distance ($z_f = 1\times 10^5$ a.u.), a decision procedure determines whether the electron remained with the target, has been transferred to the projectile, or was ejected to the continuum. The number of trajectories is chosen in such a way that the statistical error is less than 5%. Other errors, e.g., truncation and roundoff errors, were minimized by suitable choice of the parameters of the integration routine and are less than the statistical errors.

A collision event is considered ''over'' when it is no longer necessary to evolve the particle trajectories under the full three-body Hamiltonian Eq. (2.1). Asymptotically, the final state of the ion-atom collision is governed by two- and one-body Hamiltonians in the case of excitation or capture, or three one-body Hamiltonians in the case of ionization. In practice we evolve the ion-atom system until the factorization into the two- and one-body problems is possible, and evaluate the two-body total energy to determine if the two-body system will break up further, resulting in ionization. The end point z_f of the three-body propagation is chosen such that for any position of the electron at least one of the Coulomb terms in Eq. (2.1) is negligible. Thus the Hamiltonians $H_{e\text{-}T}$ and $H_{e\text{-}P}$ are defined by dropping, respectively, the Coulomb potential from projectile and target nuclei:

$$H_{e\text{-}P}=\frac{1}{2}(\vec{p}-\vec{v})^2-\frac{1}{|\vec{r}-\vec{R}|}+\frac{1}{2}\gamma l_z+\frac{1}{8}\gamma^2\rho^2 \qquad (2.22)$$

and $H_{e\text{-}T}=H_{\text{init}}$, [see Eqs. (2.2), (2.3), and (2.4)], where both are expressed in the target frame. While propagating the electron trajectory with the full Hamiltonian, the two-body interaction energies $H_{e\text{-}T}$ and $H_{e\text{-}P}$ are calculated. At z_f at least one of these energies is constant in time, and this is revealed by simply evaluating the standard deviation of both two-body energies recorded from the last thousand integration steps.

Having decided which two-body Hamiltonian best describes the final state, evaluation of its energy allows the classification of the outcome of the ion-atom collision: excitation of the target atom, ionization of the same, or capture by the projectile ion. Since l_z is a good quantum number for $H_{e\text{-}T}$, the ionization threshold energy turns out to be $\frac{1}{2}\gamma(|l_z|+l_z)$ due to the combined effect of the centrifugal and diamagnetic potentials. For Eq. (2.22) the ϕ motion cannot be separated (discussed below), resulting in an ionization threshold of zero energy. If $H_{e\text{-}T}$ is constant and less than $\frac{1}{2}\gamma(|l_z|+l_z)$, then the electron remains bound to the target nucleus. If $H_{e\text{-}P}$ is constant and less than zero, then the electron has been captured by the projectile nucleus. All other situations lead to ionization. Numerically, if N_{Tot} is the total number of trajectories and N the number of events leading to capture or ionization, the respective cross sections are

$$\sigma=\frac{N}{N_{\mathrm{Tot}}}\ \pi b_{\max}^{2}\left[1\pm\frac{\sqrt{N_{\mathrm{Tot}}^{2}+N^{2}}}{N_{\mathrm{Tot}}N}\right]. \tag{2.23}$$

The second term is the standard deviation of the estimated cross section.

The combination of charge transfer and the presence of the external magnetic field leads to a new type of atomic state. The Coulomb symmetric gauge about the target charge center must remain throughout the ion-atom collision, resulting in an *asymmetric gauge* for the electron-projectile system $H_{e\text{-}P}$; see Fig. 2. A coordinate transformation gives the Hamiltonian for the captured electron in the frame of the projectile:

$$\begin{aligned}H'_{e\text{-}P}=&\frac{1}{2}\,\vec{p}\,'^{2}-\frac{1}{|\vec{r}\,'|}+\frac{1}{2}\,\gamma l'_{z}+\frac{1}{8}\,\gamma^{2}\rho'^{2}\\&+\frac{1}{2}\,\gamma b p'_{y}+\frac{1}{4}\,\gamma^{2}bx'+\frac{1}{8}\,\gamma^{2}b^{2},\end{aligned} \tag{2.24}$$

where $\vec{r}\,'=\vec{r}-\vec{R}$ and $\vec{p}\,'=\vec{p}-\vec{v}$. Equation (2.24) is written so that the usual Hamiltonian, for an atom in a magnetic field with the symmetric gauge terms, appears on the upper line, and the additional terms introducing the asymmetry are written on the next line. The off-center paramagnetic interaction results in the term proportional to p'_{y}, while the off-center diamagnetic interaction pulls on the electron with the Stark-like term $\frac{1}{4}\gamma^{2}bx'$ and gives an overall boost in energy of $\frac{1}{8}\gamma^{2}b^{2}$. Further study of the interplay of the paramagnetic and diamagnetic terms is desirable to understand the structure of the final electronic state on the neutralized atoms.

III. RESULTS

With the method outlined above, we have calculated the cross sections for charge exchange and ionization for the $k_{\max}$ and the $k_{\min}$ states for a magnetic field strength of almost 0, 2, and 4 T. The results for ionization were previewed in [6] and are postponed to a later work [19]. For the target quantum number of $n=28$ under consideration the field of 4 T marks the upper boundary of the l-mixing region, because the diamagnetic energy becomes comparable to the energy spacing between adjacent principal quantum numbers. The breakdown of the perturbative regime for $B>4$ T is also seen in the divergence of the true magnetron period from values obtained from Eq. (2.19). In contrast there is no lower physical limit in the magnetic field strength for the initial-state construction with the method explained above, because the eigenstates are independent of the field strength [see Eq. (2.5)]. But there is a practical limit because the time to reach the initial electron coordinate becomes too large for $\lim_{B}\rightarrow 0$, as can be seen by the scaling law from Eq. (2.19).

On the other hand the infinitely long magnetron period for $\lim_{B}\rightarrow 0$ offers an alternative way to construct the electron initial-state distribution and to verify the classical approach. In the quasi-field-free case the electrons are moving on an unperturbed Kepler ellipse and the drift of the elliptical parameters is negligible. Therefore the initial-state distribution can be accomplished by a superposition of l states statistically weighted according to the desired l distribution. In the limiting case of a vanishing magnetic field strength it is possible to gain a stationary initial phase-space distribution even for the quantum-mechanical l distribution. This holds because the negligible field strength causes no change of the l expectation value within the time scale considered here; especially no change of the overall distribution from the quantum mechanical towards the classical one will occur, as seen in higher field cases. Utilizing this feature, we have performed total cross section calculations for $B\approx 0$ in which the l distribution of the collision ensemble is identical to the quantum mechanical and the classical l distribution (cf. Fig. 5). In spite of the apparent discrepancies of the quantum and classical phase-space distributions (cf. Fig. 4) the results of both sets agree closely, giving further confidence in the classical approach. A more sensitive quantity, such as a differential cross section, might detect a discrepancy, though.

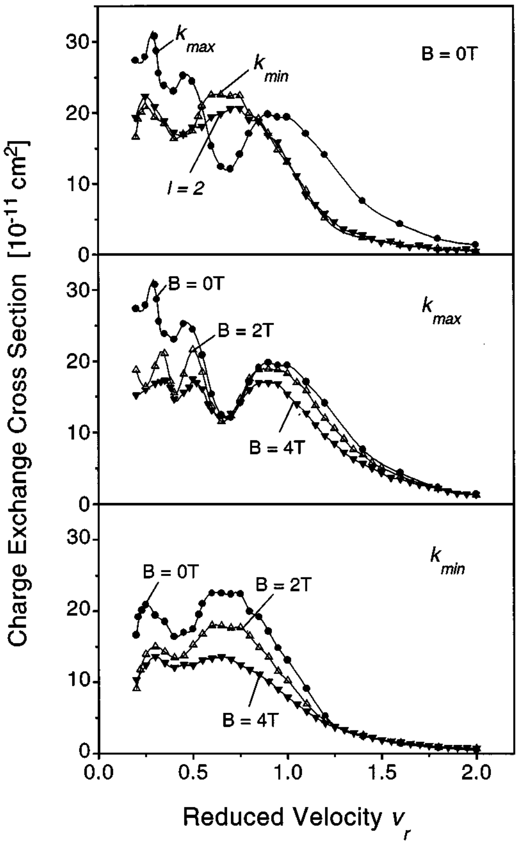

FIG. 6. Capture cross sections for the field-free case (upper), $k_{\max}$ (middle), and $k_{\min}$ states (lower). The upper panel reveals the ''structure effect,'' while the middle and lower panels identify the direct influence of the magnetic field on the exchange dynamic. To guide the eye the data are interpolated (solid line).

The results for capture are shown in Fig. 6. Clearly, a significant change of the capture cross section caused by the magnetic field on can be seen. To further specify the influence of the magnetic field on the collision process, one must distinguish between two effects. First, the applied magnetic field changes the target electron starting distribution, (see

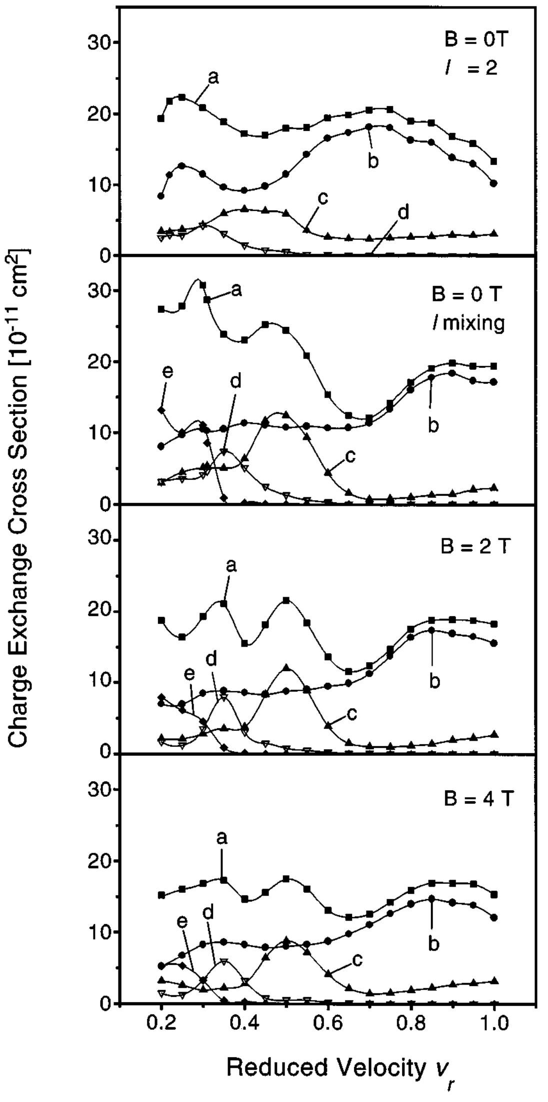

FIG. 7. Total capture cross sections (a) for $l=m=2$ (upper) and $k_{\max}$ states resolved for the contributions from one-swap (b), three-swap (c), five-swap (d), and ⩾seven-swap (e) processes. To guide the eye the data are interpolated (solid line).

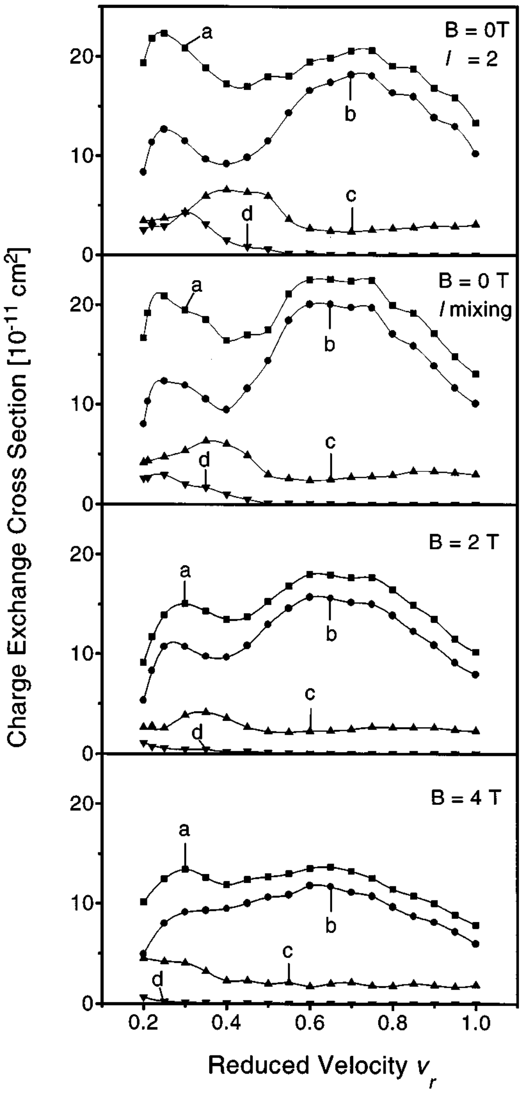

FIG. 8. Total capture cross sections (a) for $l=m=2$ (upper) and $k_{\min}$ states resolved for the contributions from one-swap (b), three-swap (c), and five-swap processes (d). To guide the eye the data are interpolated (solid line).

Fig. 4) and, second, the dynamics during the collision are directly affected by the magnetic field. In order to differentiate between the two, we compare the cross sections for capture from the $k_{\max}$ and $k_{\min}$ states at $B\approx 0$, 2, and 4 T with the $l=2$, $m=2$ state. All states can be produced by a two-photon excitation process where the $l=m=2$ state is excited in the field-free case.

The ''structure effect,'' i.e., the influence of the changed initial electron distribution in the magnetic field becomes apparent if one compares at $B\approx 0$ the cross section for a $l=2$ state with those for $k_{\max}$ and $k_{\min}$ (Fig. 6, upper graph). Little difference is seen between $l=2$ and $k_{\min}$; this can easily be understood since $l=2$ provides also the major contribution to the quantum-mechanical $k_{\min}$ state (cf. Fig. 5, lower graph). Both states, $l=2$ and $k_{\min}$, are more or less disk-shaped, orientated parallel to the field direction. In contrast, the difference between $l=2$ and $k_{\max}$ is quite marked; the curve for $k_{\max}$ is shifted to higher v_r and as a consequence a third peak at very low v_r appears in the viewed velocity region. The shift in the cross sections between the field states $k_{\max}$ and $k_{\min}$ can be understood by comparing with the analogous field-free cases. The $l=12$ and $l=2$ harmonics are the largest components of the $k_{\max}$ and $k_{\min}$ states, respectively (see Fig. 5), and the same shift is observed between these field-free cases, which can be understood by a velocicty matching argument: In the $l=2$ case the orientation is nearly parallel with the quantization axis (z direction) for $m=2$, which indicates that the electron current flows perpendicular to the projectile ion path with weak linear momentum components along the collision (z) axis. For $l=12$, $m=2$ the orientation points approximately perpendicular to the z axis, resulting in part of the initial-state electron current running with the incoming ion and thus introduces strong linear momentum components along the collision axis. Thus for the $l=12$ initial state there is a greater possibility for capture at higher velocities. Since the exchange cross sections for $k_{\max}$ ($k_{\min}$) and $l=12$, $m=2$ ($l=m=2$), respectively, are rather similiar and the l values are the most probable out of the corresponding l distribution, this indicates that the same reasoning is valid for the electron capture in a magnetic field. For example, at $v_r = 1$ the collision velocity is $v = 0.036$ a.u.; as can be seen from Fig. 4 (upper right graph) $p_z(k_{\max})$ is quite intense around this value, but far out of the range for $k_{\min}$. Therefore, the conditions for charge exchange are most favorable for $k_{\max}$ particularly at $v_r \geqslant 1$. This comparison of $k_{\max}$ and $k_{\min}$ is similiar to the one seen when keeping l fixed and going from high to low m [20].

The direct influence of the magnetic field on the charge exchange dynamics for the $k_{\max}$ and $k_{\min}$ states can be seen in the middle and lower panel of Fig. 6, respectively, since the l composition (structure) of the states remains unchanged in the magnetic field range under consideration. The direct influence of the magnetic field does not alter the overall structure of the exchange cross sections with respect to field strength, but only the amplitude. For both states the exchange cross section is decreased at $v_r < 1$ with increasing magnetic field, while at $v_r > 1.25$ ($k_{\min}$) and $v_r > 1.5$ ($k_{\max}$) the capture is fairly unaffected by the field strength.

Analyzing the features of the exchange cross sections in more detail, we examine now the peaks found at low impact velocities. In the field-free case these peaks have been identified by MacAdam and co-workers [21] as the contribution of one swap, three swaps, and higher-order swaps (i.e., passage of the electron through the projectile-target midplane) to the exchange cross section; the order of swaps characterizes how often the electron passes through the target-projectile midplane before it finally stays with the projectile. In Figs. 7 and 8 we present the exchange cross sections for different magnetic field strengths resolved for the various swaps. The two top panels in both figures show the ''structure effect'' already discussed above: At $B \approx 0$ the pure $l = 2$ state behaves similar to the $k_{\min}$ state, while it is quite different from $k_{\max}$. In Fig. 7 every peak in the total exchange cross sections for $k_{\max}$ states can be traced back to a specific order of swaps. The width and position of the different swap peaks are practically the same for all $k_{\max}$ states, independent of the applied magnetic field. The cross sections are seen to decrease as the field increases, especially for the highest-order swap, probably due to the electron path bending out of the collision plane as it travels between the two nuclei.

For the $k_{\min}$ state (Fig. 8), the one-swap process comprises the main contribution to the total capture cross section over the whole velocity range. There is also a fairly flat three-swap curve and a much reduced contribution from five-swap processes, while higher-order swaps are negligible in this velocity range, and are therefore not shown in the figure. We also note that the higher-order swap contributions peak at a velocity lower than the corresponding $k_{\max}$ curves. This is most likely due to the different interaction length of the $k_{\min}$ state, reflecting the ''structure effect.'' These shifts also depend on the order of the swap and the applied magnetic field strength, indicating that this is caused by the direct influence of the magnetic field on the exchange dynamics. Further investigation into the charge-transfer mechanisms should prove interesting.

IV. CONCLUSION

The initial-state method presented in this paper marks a significant advance for CTMC calculations. It is now possible to create a classical ensemble that simulates a quantum state for a Hamiltonian with *two nonseparable degrees of freedom*. The method generalizes to initial-state systems that can be analyzed by perturbation theory. Applied to the problem of charge transfer in a magnetic field, the new CTMC method reveals exchange mechanisms similar to the field-free electron transfer for ions colliding with Rydberg atoms. The effect of the magnetic field is twofold: Firstly, in the l-mixing regime, high l components are mixed into the corresponding field-free $n = 28$, $l = m = 2$ state, leading to a set of new states k, which concerning their phase space distribution fall apart into a prolate and oblate geometry. Particularly in the strongly elongated $k_{\max}$ state, this introduces high linear momenta parallel to the collision direction while the disk-shaped $k_{\min}$ state does not behave much differently from the field-free $l = 2$, $m = 2$ state. Secondly, the field also affects the dynamics of the electron exchange process, mainly reducing its probability, and thus the total cross section. This is supposedly due to the Lorentz force, which diverts the electron from a Coulomb trajectory. The effect is particularly noticeable for the $k_{\min}$ state, where a 4-T field causes a cross-section reduction of as much as 50%. In addition, the contribution of the various processes classified by the number of swaps exhibits much different behavior for the $k_{\min}$ capture cross sections. Finally we point out that the calculations presented here made possible an analysis of ion–Rydberg-atom collisions in a magnetic field for an experimentally accessible range of parameters.

[1] P. Zeeman, Philos. Mag. **5**, 43 (1897).

[2] S. Suzuki, N. Shimakura, and M. Kimura, J. Phys. B **29**, 1063 (1996).

[3] S. Bivona and M. R. C. McDowell, J. Phys. B. **20**, 1541 (1987).

[4] U. Wille, Phys. Lett. A **125**, 52 (1987).

[5] T. P. Grosdanov and M. R. C. McDowell, J. Phys. B **18**, 921 (1985).

[6] S. Bradenbrink, E. Y. Sidky, Z. Roller-Lutz, H. Reihl, and H. O. Lutz, J. Phys. B **30**, L161 (1997).

[7] R. Abrines and I. C. Percival, Proc. Phys. Soc. **88**, 861 (1966); **88**, 873 (1966).

[8] J. Wang and R. E. Olson, Phys. Rev. Lett. **72**, 332 (1994).

[9] D. M. Homan, M. J. Cavagnero, and D. A. Harmin, Phys. Rev. A **51**, 2075 (1995).

[10] S. Bradenbrink, H. Reihl, Z. Roller-Lutz, and H. O. Lutz, J. Phys. B **28**, L133 (1995).

[11] C. O. Reinhold and C. A. Falcón, Phys. Rev. A **33**, 3859 (1986).

[12] H. Friedrich, *Theoretical Atomic Physics* (Springer, Berlin, 1990).

[13] U. Fano, F. Robicheaux, and A. R. P. Rau, Phys. Rev. A **37**, 3655 (1988).

[14] P. A. Braun, Zh. Eksp. Teor. Fiz. **84**, 850 (1983) [Sov. Phys. JETP **57**, 492 (1983)].

[15] E. A. Solov'ev, Zh. Eksp. Teor. Fiz. **82**, 1762 (1982) [Sov. Phys. JETP **55**, 1017 (1982)].

[16] J. S. Cohen, Phys. Rev. A **26**, 3008 (1982).

[17] R. E. Olson and A. Salop, Phys. Rev. A **16**, 531 (1977).

[18] H. Herold, H. Ruder, and G. Wunner, J. Phys. B **14**, 751 (1981), and references therein.

[19] S. Bradenbrink, E. Y. Sidky, Z. Roller-Zutz, H. Reihl, and H. O. Lutz, J. Phys. B **30**, L161 (1997).

[20] Th. Wörmann, Z. Roller-Lutz, and H. O. Lutz, Phys. Rev. A **47**, R1594 (1993).

[21] K. B. MacAdam, J. C. Day, J. C. Aguilar, D. M. Homan, A. D. MacKellar, and N. J. Cavagnero, Phys. Rev. Lett. **9**, 1723 (1995).